Materials Research. 2023; 26: e20220606
DOI: https://doi.org/10.1590/1980-5373-MR-2022-0606

Surface Microstructure Refinement and Mechanical Properties of GCr15 Steels Improved During Ultrasonic Surface Rolling Processing

Xianmeng Xue[a], Shubo Xu[a,b*], Xiquan Ma[a], JuanJuan Han[a], Wei Zheng[a]

[a]Shandong Jianzhu University, School of Materials Science and Engineering, Jinan, 250101, China.
[b]Central China University of Technology, State Key Laboratory of Material Forming and Mould & Die Technology, Wuhan, 430025, China.

Received: December 18, 2022; Revised: January 25, 2023; Accepted: February 01, 2023

In this paper, ultrasonic surface rolling processing (USRP) was used to strengthen GCr15-bearing steel. A finite element three-dimensional model of USRP was established to analyze the residual compressive stress and equivalent plastic strain distribution on the bearing steel surface. The microstructure, hardness, surface roughness, and corrosion resistance before and after USRP treatment were characterized by SEM, EBSD, X-ray diffraction (XRD), and electrochemical techniques. Results indicated that USRP treatment can significantly improve the material's surface microstructure and residual compressive stress distribution and obtain a plastic strain layer of about 60μm. After USRP treatment, the Kernel Average Misorientation (KAM) increased, and the dislocation activity was more intensive, resulting in aggregation near grain boundaries, and the percentage of LAGBs increased to 38.8%. Under the combined effect of surface grain refinement, residual compressive stress, and high glossy surface, the self-corrosion current density is reduced by two orders of magnitude, and the corrosion resistance is significantly improved. This investigation suggests a solution to the bearing failure problem and has implications for understanding the deformation mechanism of ultrasonic surface rolling processing.

Keywords: *GCr15, ultrasonic surface rolling process (USRP), grain refinement, hardness, corrosion resistance.*

1. Introduction

As one of the most commonly used high chromium bearing steels, GCr15 steel (AISI-52100) has good hardness, strength, wear resistance, and corrosion resistance. It has been widely used in manufacturing bearing rings, ball screws, molds, and other complex mechanical parts[1,2]. However, the surface organization of GCr15 steel is sensitive to failure behavior. Under harsh conditions of use, the surface is prone to wear and fatigue, and other failures, affecting the service life of the parts and wear resistance, which seriously affects the safe use of the equipment and restricts the development of the high-quality industry[3]. Therefore, to improve the surface mechanical properties of GCr15, the surface peening techniques (such as Deep Rolling Strengthening[4], Shot Peening[5,6], Ultrasonic Shot Peening[7,8], Laser Shock Peening[9,10] and Ultrasonic Surface Rolling[11,12]) have been put forward with higher requirements. Surface strengthening techniques can improve the surface microstructure, surface roughness, and stress state of the part, and significantly improve the part's corrosion resistance, wear resistance, fatigue performance, and service life[12-14].

Surface strengthening techniques reduce surface roughness, thus inhibiting crack generation and controlling the surface microstructure[15]. On the one hand, the surface strengthening technique introduces a gradient residual compressive stress field on the material surface, which inhibits or slows down the sprouting of fatigue cracks. On the other hand, the refinement of surface grains and grain boundaries increase also helps inhibit crack extension. Ultrasonic Surface Rolling Processing (USRP) has enhanced surface properties[16-18]. During the USRP process, ultrasonic vibration caused severe plastic deformation and formed a residual compressive stress layer on the material surface, which inhibited crack expansion. It also refined the surface grains[19].

Wang et al.[20] showed that USRP treatment of M50 steel formed a plastic deformation layer of 24μm thickness, and fine grain strengthening increased the alloy hardness by 15.56%, increased residual stress by 79.61%, and reduced surface roughness by 68.09%, transforming the primary wear mechanism to slight adhesive wear. Zou et al.[21] showed that after multiple UNSM treatments of DZ2 shaft steel, the near-surface grain refinement of DZ2 shaft steel. The surface residual compressive stress increased from -73 MPa to -703 MPa, and the wear resistance of the specimens treated with three passes of UNSM under sliding conditions was significantly enhanced. Dong et al.[22] showed that the ultrasonic surface rolling process (USRP) treatment of 300M steel resulted in a highly smooth surface finish, introduced significant residual compressive stresses, increased surface hardness by about 30.9%, and significantly improved its wear resistance. Yang et al.[23] investigated the grain growth mechanism of GH4169 high-temperature alloy by excessive ultrasonic surface rolling. They found that the collective migration of adjacent grain boundaries caused by excessive cyclic plastic deformation promoted the formation of nanotwins.

*e-mail address:xsb@sdjzu.edu.cn

Currently, the research on GCr15 steel mainly focuses on surface chemical heat treatment[21,22]. These studies mainly focus on carburizing, nitriding, and other treatments. Most of these surface strengthening techniques use the process of shot blasting[24], hard turning[25] and other surfaces. Fu et al.[26] studied the variation of surface XRD half maximum width (FWHM), residual stresses and hardness with annealing time and temperature of GCr15 steel after three times shot blasting (TSP). Modern industrial production levels have placed higher demands on the performance of GCr15 bearing steel. In this paper, a three-dimensional finite element processing model of USRP was developed using ultrasonic surface rolling technique to analyze the residual compressive stress and equivalent plastic strain distribution on the bearing steel surface. The microstructure, hardness, surface roughness and corrosion resistance of USRP before and after treatment were characterized by SEM, EBSD, X-ray diffraction (XRD) and electrochemical testing techniques, and the microstructure change mechanism of USRP was analyzed to provide a reference for surface modification of GCr15 bearing steel. To provide a safe and reliable process technology solution for bearing life improvement.

2. Materials and Experimental Methods

2.1. Materials

The material used in this study was GCr15-bearing steel (AISI-52100), whose main chemical composition is shown in Table 1. The material is made into a specimen of 30mm in diameter and 50mm in length by EDM. Heat treatment of the material was carried out with a heat treatment process of 860°C±10°C, holding 30 min oil quenching and 150°C±10°C tempering for 2 h. The average surface roughness of the obtained specimens was 0.25μm, and the measured surface hardness was 697$HV_{0.5}$.

2.2. Finite elements models of USRP

The ultrasonic surface rolling processing was numerically simulated using Abaqus/Explicit software. The geometry of the workpiece was an annular specimen of Φ30 mm × Φ25 mm × 5 mm. The ultrasonic rolling head was a Φ10 mm ball (Figure 1). The deformed workpiece was calculated as an eight-node linearly reduced integration unit (C3D8R), and one-eighth of the deformed workpiece was taken to improve the efficiency of the operation. The minimum cell size on the contact surface in the machining area was 0.05 mm, and the grid in the non-machining area was relatively large. In addition, the workpiece is rotated around the central axis of rotation (Z-axis), which imposes on the tool head a velocity in the negative Z-axis direction and a displacement of periodic vibration in the Y-axis direction. The contact type between the tool head and the workpiece was surface-to-surface contact with a friction coefficient of 0.1

The workpiece and ultrasonic rolling tool head materials were GCr15-bearing steel, and YG8 cemented carbide, respectively. The difference in modulus of elasticity between the cutter head and the material was so significant that the ultrasonically rolled cutter head was defined as non-deformable (rigid body). The workpiece material was GCr15 steel, and the Johnson-Cook equation set the material plasticity parameters. The Johnson-Cook equation can describe the work-hardening effect exhibited by GCr15 steel at different strain rates. Table 2 describes the J-C model parameters of the steel containing GCGCr15 and Table 3 describes the physical parameters of the material.

Static pressure and ultrasonic vibration conversion produce dynamic impact force applied to the surface of the workpiece. At the same time, the dynamic impact force changes as a sine function. The dynamic impact force with the regular variation of the sine function can be calculated by Equation 1:

$$\varphi(t) = A_0 + \sum_{n=1}^{\infty} (a_n \cos(n\omega t) + b_n + \sin(n\omega t)) \quad (1)$$

Where A_0 is a constant term, n is the number of harmonics, a_n, b_n is the harmonic amplitude, and ω is the angular frequency of the dynamic shock wave, $\omega = 2\pi f$, where f is the frequency of the ultrasonic vibration. Since the vibration is a sine wave, the equation A_0=0, n=1, a_n=0, b_n is the amplitude of ultrasonic vibration.

2.3. USRP experiment

The USRP system processed the specimen (HK30G equipped with an HS actuator, China). The rolling tool

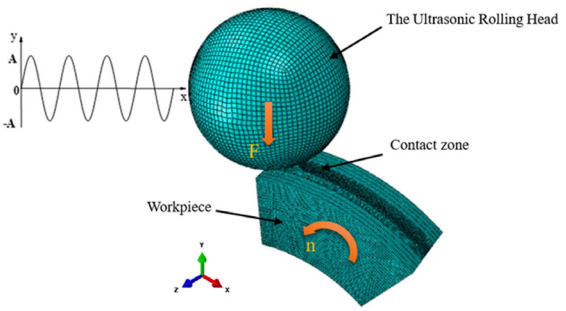

Figure 1. Finite element model of the ultrasonic rolling process.

Table 1. Main chemical composition of GCr15 steel (wt%).

C	Mn	Si	S	P	Cr	Fe
0.95-1.05	0.20-0.40	0.15-0.35	≤0.02	≤0.027	1.30-1.65	Bal.

Table 2. GCr15 bearing steel J-C model parameters.

A/MPa	B/MPa	C	m	n
1744	1440	0.03	0.66	0.19

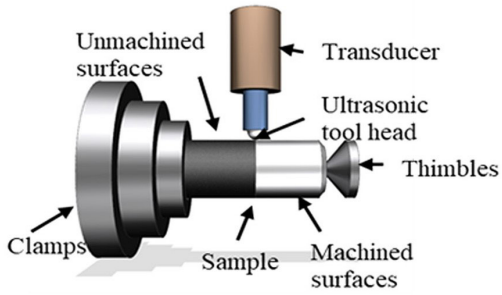

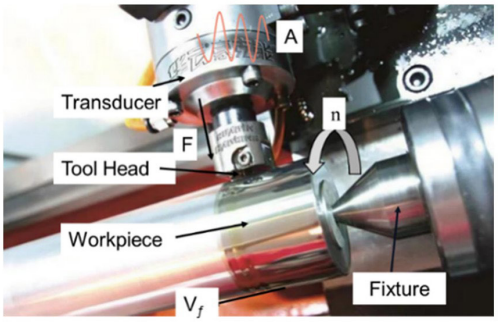

Figure 2. Ultrasonic surface rolling processing chart.

head mainly consisted of the transducer, variable amplitude rod, and impact head, which was mounted on the CNC lathe table to complete the processing of the specimen by rotating the machine. Figure 2 shows the physical picture of USRP processing. During the USRP process, the specimen surface experienced an extrusion pressure generated by a combination of continuous rolling and ultrasonic vibration of the impact head. The tool head was a 10 mm diameter sphere of tungsten carbide metal that overlapped vertically with the material surface. The tool head emits ultrasonic vibrations and static pressure in a fixed direction and rolls at an appropriate speed to transfer the static and dynamic pressure to the material surface.

Specimens with a geometry of 5 mm × 10 mm × 10 mm were hand-ground and mechanically polished in cross-section and eroded with 4% nitric acid alcohol solution. The microstructures were observed using optical microscopy (OM; VHX-2000), scanning electron microscopy (SEM; ZEISS SUPRA 55), and electron backscatter diffraction (EBSD; ZEISS SUPRA 55). EBSD data were analyzed using OIM Analysis software. The gradient hardness of the specimen sections before and after USRP treatment was measured using a Vickers hardness tester (HVS-1000A) with a load of 4.89 N (0.5 kg) and a holding time of 15 s. The residual stress test was measured and calculated using a blind hole stress detector (HK21A). According to this method's measurement principle, the hole's slight deformation during stress release is sensed by strain gauges, and the corresponding residual stress is further calculated by the strain of the hole measured by resistance strain gauges. The surface samples were identified using an x-ray diffractometer (XRD, Rigaku smartlab) at 45 kV and 40 mA of Cu-Kα radiation (λ = 1.54056 Å). Diffraction data were collected in the 2θ range of 20◦-90◦ at a scan rate of 2◦/min. The Tafel curves of the material before USRP treatment were measured using an electrochemical workstation (Interface 1000) to calculate the material's corrosion resistance. The working electrode is the GCr15 sample, the reference electrode is saturated with glycury, the auxiliary electrode is a platinum sheet electrode, the corrosive environment is 3.5% NaCl solution (wt%), and the working temperature is 20°C±2°C. The surface morphology of the sample was characterized using a laser spectroscopic confocal microscope (KC-X1000) with a measurement area of about 5 mm × 5 mm, and the linear roughness values Ra and Rz were measured along the axial direction of the sample. The schematic diagram of electrochemical experiments and SEM specimen preparation is shown in Figure 3.

Table 3. Physical properties of materials.

Material	Density (g/cm^3)	Elastic Modulus (Gpa)	Poisson's ratio
GCr15	7.83	219	0.29
YG8	14.5	510	0.3

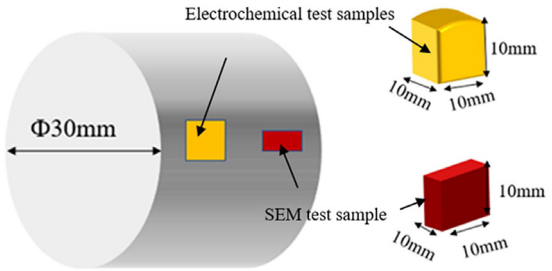

Figure 3. Schematic diagram of electrochemical experiments and SEM specimen preparation.

3. Results and Discussion

3.1. Finite element simulation results

The residual compressive stress inhibits the sprouting and expansion of surface cracks, which can improve their surface properties, thus improving the overall mechanical properties of the engineered parts. From the Miss stress cloud and equivalent plastic strain diagram (Figure 4), it can be found that the residual stress tends to increase and then decrease along the surface depth. The maximum residual stresses are not on the upper surface of the material but on the secondary surface. The elastoplastic deformation of the surface during the USRP treatment caused this. After recovery of the elastic deformation, the residual stresses on the surface were released, and the resulting plastic deformation resulted in the maximum residual stresses on the secondary surface.

The elevation of residual stresses is attributed to the combination of static pressure and ultrasonic vibration

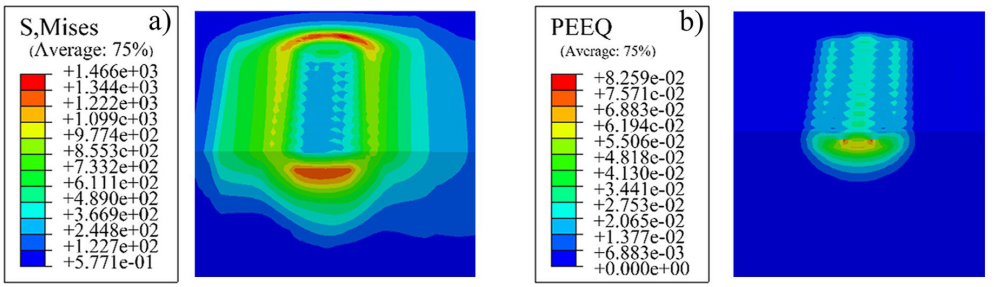

Figure 4. Miss stress cloud (a) and equivalent plastic strain diagram (b).

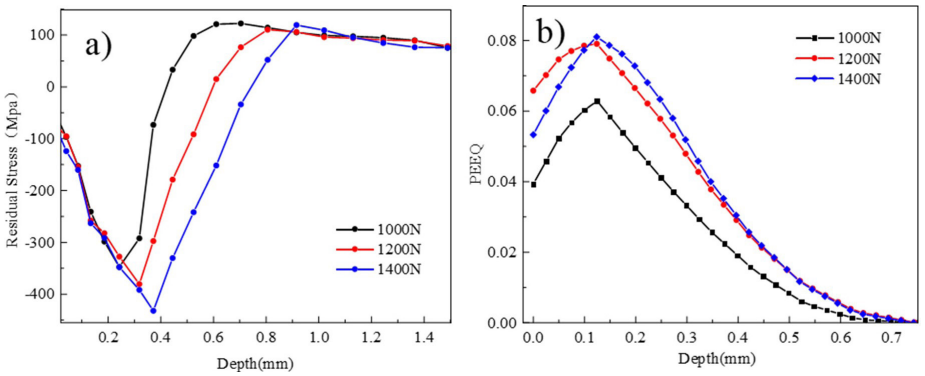

Figure 5. Distribution of residual stress and equivalent plastic strain along the depth direction under different static loading forces (1000N, 1200N, 1400N).

Table 4. USRP experimental process parameters.

Ultrasonic vibration frequency (kHz)	28
Ultrasonic vibration amplitude (μm)	8
Static force (N)	1000
Rotation speed of sample (rpm)	160
Feeding speed (mm/r)	0.08

forces acting on the machined surface, which results in severe plastic deformation and surface nanosizing effects. Finite element analysis was carried out using ABAQUS/Explicit. The effect law of USRP treatment on the residual stress and plastic deformation of GCr15 steel under different static pressures (1000N, 1200N, 1400N) was investigated. The maximum residual compressive stresses reached 347 Mpa, 380 Mpa, and 432.04 Mpa, respectively, as the depth continued to increase (Figure 5a). Figure 5b shows that the plastic deformation tends to increase and then decrease from the figure. The greater the static pressure, the greater the PEEQ, the more severe the surface plastic deformation, and the deeper the plastic deformation.

The samples treated with the parameters in Table 4 were tested by the blind hole method, and the simulation results and test results of the residual stress are shown in Figure 6. The finite element calculation results agree well with the experimental values, and the average error is less than 6.8%, which is within the acceptable range. These errors are due to the inhomogeneity of the internal microstructure or the material's phase change after heat treatment. Figure 6 shows

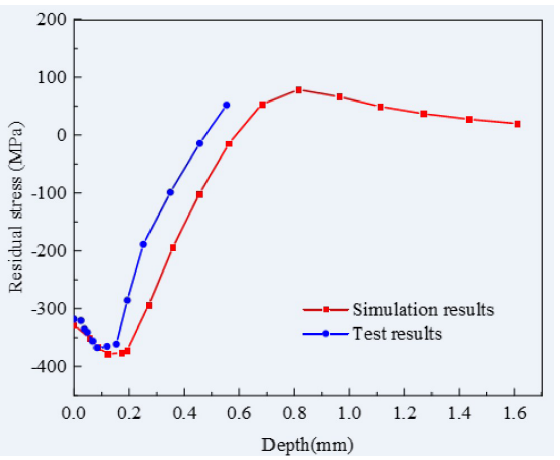

Figure 6. Distribution of residual stress on the specimen surface with depth.

that the trend of the finite element calculation results along the depth direction is highly consistent with the experimental measurements, thus providing solid theoretical support for the USRP analysis.

3.2. Microstructural characterization

The microstructure of the surface layer of the USRP front and rear shaft steel is shown in Figure 7. From the optical microscope image (Figure 7a), it can be seen that the

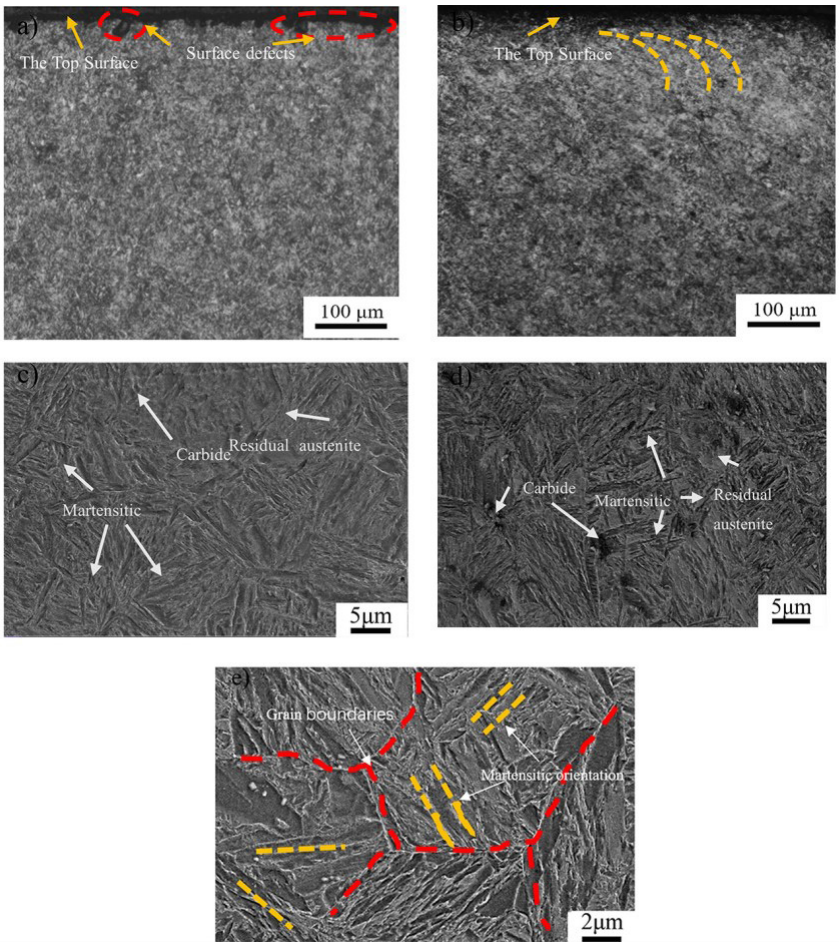

Figure 7. Microstructure of the surface layer of axial steel before and after USRP. (a) Untreated microstructure (OM); (b) USRP treated microstructure (OM); (c) Untreated microstructure (SEM); (d) and (e) USRP post microstructure (SEM).

original tissue surface of GCr15 GCr15-bearing has large carbide particles, pits, and other defects, which are usually the source of stress concentration areas and crack sprouting. After treatment with USRP, the specimens can be found under the optical microscope (OM), where the surface pits disappeared, and the surface quality was greatly improved. The blurring of the microstructure at a thickness of about 10μm from the top surface under an optical microscope (OM) at the same magnification (Figure 7b) is due to the coupling of plastic deformation and high shear stress, static pressure, and ultrasonic vibration at high strain rates in USRP resulting in refined surface grains. The original grains under the surface layer were compressed and elongated in the rolling direction, indicating that a plastic deformation layer about 60μm thick was formed during the USRP treatment due to the coupling effect of static pressure and ultrasonic vibrations that exceeded the yield strength of the material. However, the changes within the plastic deformation layer along the rolling direction were not noticeable when observed under the optical microscope. The main reason is that the study material has high strength and hardness, and the impact density provided by only one USRP treatment is difficult to induce a considerable enough deformation to produce significant grain refinement. Moreover, Li et al.[27] reported that the plastic deformation phenomenon changes more significantly when dealing with soft materials.

Figure 7 shows SEM images of the cross-sectional microstructure of GCr15 bearing stGCr15-bearing after USRP. As can be seen from Figure 7c, the steel is mainly composed of martensite, residual austenite, and a tiny amount of diffuse distribution of carbide particles. The martensite shape is mostly flaky. After the USRP treatment (Figure 7d), the top surface martensite became significantly smaller, and the martensite orientation in the plastic deformation layer became disordered. This can be attributed to the grain refinement phenomenon caused by the coupling effect of ultrasonic vibration and static pressure in which the martensite tissue is broken. The secondary surface layer of the material, due to the increase in depth, does not introduce enough kinetic energy to cause grain refinement, and the martensitic organization within the grain is elongated. In the high-magnification SEM image (Figure 7e), the red curve represents grain boundaries and the orange curve represents martensitic orientation. It was found that martensitic tissue in the grain appeared staggered in different orientations, which were limited to the interior of the grain, and the area

of the interlaced zone was considered to be the deformation zone. This is similar to the results also reported by other researchers[23,28].

3.3. Plastic deformation and grain refinement analysis

Using the EBSD technique, specimens were described to more thoroughly examine the impact of plastic deformation and grain refinement on the surface of GCr15 before and after USRP treatment. It is challenging to distinguish micro- and nanoscale microstructures in the top machined region in EBSD maps because of the severe plastic deformation brought on by the coupling of static pressure and ultrasonic vibrations on the material's top surface. Therefore, microstructures with a surface depth of approximately 10 um were selected for scanning. The outcomes of the EBSD study before and after USRP processing are displayed in Figure 8. (IPF map). EBSDs of micro- and nanostructures without indexing is seen in the black areas. Refined grains surround the original grains in the plastic deformation layer, as shown in Figure 8b. It illustrates how the coarse grain structure on the material surface eventually tends to the nanoscale level following severe plastic deformation in a particular direction during USRP under the repeating action of the applied load. After the USRP treatment, the number of dark spots on the surface increased, indicating that the material surface suffered significant plastic deformation that resulted in an unidentifiable refinement of the grain organization.

Figure 9 displays the samples' statistical plots and kernel average misorientation (KAM) before and after USRP treatment. Based on the average angle of local grain misorientation, KAM can determine the extent of local plastic deformation. It displays the typical relationship between a given point and its closest neighbors, also part of the exact grain[29]. In the KAM map, the blue color is associated with lower local orientation angles, and the red color is associated with higher local orientation angles. Higher KAM values indicate a higher density of dislocations within the grains. From Figure 9, it can be found that the proportion of high dislocation density regions in the USRP-treated specimens gradually increases. Most of the local dislocation angles in the surface region of the untreated material are distributed in the middle region of the martensitic organization, which may be related to the quenching heat treatment of the GCr15 steel. Quenching transforms the material's crystal structure from fcc to bcc and distorts the lattice, thus increasing the internal dislocation density of martensite. After USRP treatment, the KAM in the surface region of GCr15 steel increased significantly, mainly distributed near the grain boundaries, which can be attributed to the severe plastic deformation of the surface microstructure caused by USRP treatment the dislocation activities were more intensive and clustered near the grain boundaries.

To quantify the differences in surface local orientation errors, further ESBD was performed, and statistical analysis was performed as shown in Figure 9a' and Figure 8b'. The Kernel Average Misorientation of the USRP-treated material surface (average 1.29°) is significantly larger than that of the untreated Kernel Average Misorientation (average 0.95°). The high KAM values of the deformed grains can be attributed to the high density of dislocations generated during the USRP process. Therefore, it can be predicted that the strain-induced dislocations increase significantly after USRP processing. The positive correlation between KAM and the geometrically necessary dislocation density ρ_{GND} is calculated by Equation 2[30-32]:

$$\rho_{GND} = \frac{\alpha KAM}{bR} \tag{2}$$

Where α is the material constant, KAM is the Kernel Average Misorientation, b is the Burgers vector, and R is the scan step size. The mean value of the density is linearly related to the degree of plastic deformation of the material, which explains the maximum plastic deformation of the surface layer after treatment in a gradient distribution.

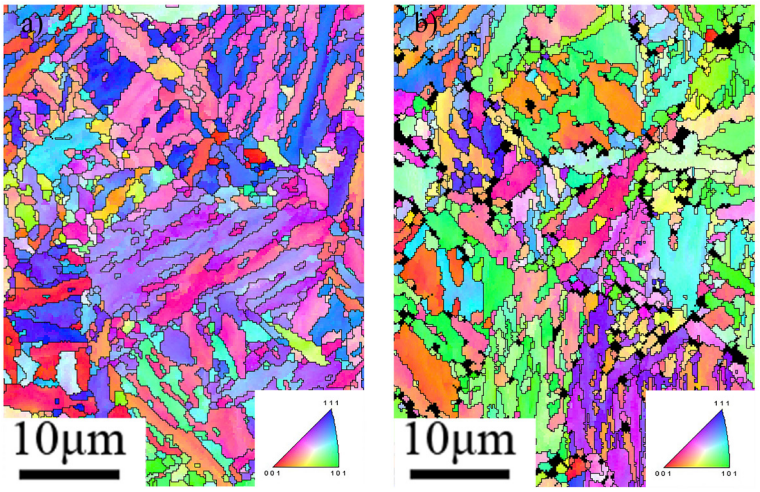

Figure 8. EBSD analysis results before and after USRP treatment (IPF plots): (a) untreated (b) USRP treated.

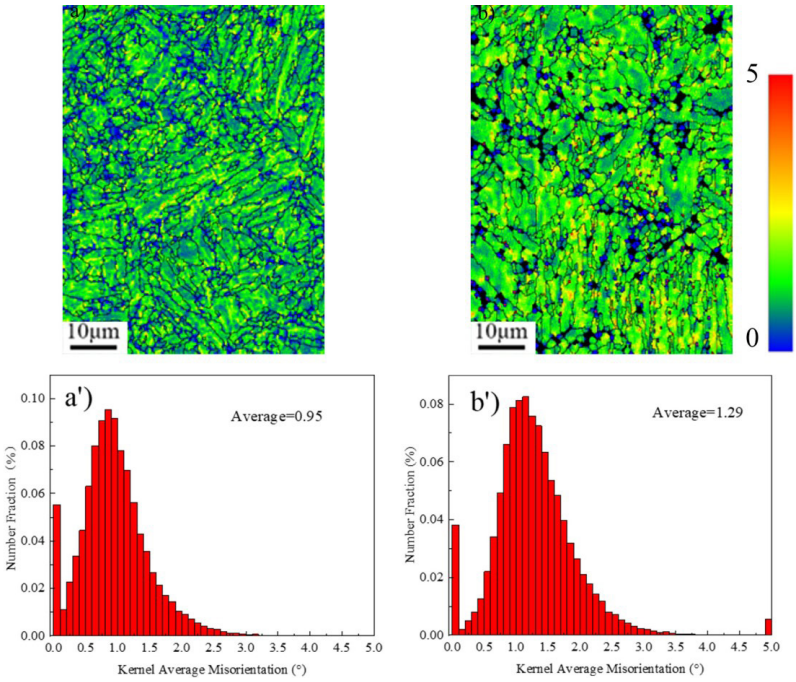

Figure 9. KAM histograms of samples before and after USRP treatment and their statistical plots: (a) and (a') untreated specimens; (b) and (b') USRP treated specimens.

Figure 10 shows the grain boundary maps and orientation angle distribution curves of the material surface before and after the USRP treatment. Low-angle grain boundaries (LAGBs, 2°-15°) are shown as green lines, and high-angle grain boundaries (HAGBs, >15°) are shown as black lines. For the untreated sample (Figure 10a), the LAGBs are randomly distributed among the HAGBs. From the corresponding orientation angle distribution curves (Figure 10a'), it can be seen that the grain boundaries show a bimodal distribution, with LAGBs and HAGBs equally prominent, and the percentage of LAGBs is about 20.2%. After the USRP treatment (Figure 9b), the surface grain was significantly deformed along the rolling direction, and the superficial LAGBs were increased considerably. In the USRP-treated material, the percentage of LAGBs increased to 38.8%, and the intensity of the HAGB distribution peak was significantly reduced from the orientation angle distribution curve (Figure 10b'). Due to the high strain and high strain rate caused by USRP, the martensitic laths are prone to many internal dislocations. Xu et al.[33] reported that dislocation accumulation is the leading cause of elevated grain LAGB. With further plastic strain development, dislocation accumulation gradually evolves into dislocation cells and entanglement, which are transformed into edges with more minor orientation deviations by annihilation and rearrangement. The migration of dislocations from the cell interior to the cell wall and the accumulation of dislocations in the HAGB lead to the continuous generation of LAGB, which results in grain refinement. In addition, under high shear deformation, the grains rotate in the rolling direction, which is responsible for the increased number of HAGBs[34].

3.4. Hardness analysis

High dislocation density and refined grains in the near-surface region lead to surface strengthening. Figure 11 shows the hardness distribution. The hardness of the untreated sample surface is about 697 $HV_{0.5}$, with a slight gradient variation along the depth. It is caused by quenching heat treatment. The quenching treatment gradually transforms the internal organization of the bearing steel GCr15 into an unbalanced organization of martensite, bainite and residual austenite. Due to the uneven distribution of quenching temperature, the microhardness values show a small gradient distribution from the surface to the core. The hardness of the USRP-treated samples increased significantly, with the maximum near-the-surface hardness of about 776 HV0.5, which was 11.33% higher than that of the substrate, but gradually decreased with increasing depth. The plastic deformation affects the hardness to a depth of about 600μm.

According to the Hall-Petch relationship, grain refinement increases hardness. The USRP-treated specimens show a significant gradient change in hardness, which is attributed to the combined effect of static pressure and ultrasonic vibration leading to work hardening and grain refinement of the violently plastic deformation layer.

In Ultrasonic Surface Rolling, the deformation of the material is caused by the movement of dislocations, and the increase in dislocation density leads to the process hardening of its surface; therefore, the relationship between hardness and dislocation density can be expressed by the following equation[35,36]:

$$H_V = \frac{Gb_1}{K}\sqrt{\rho} \tag{3}$$

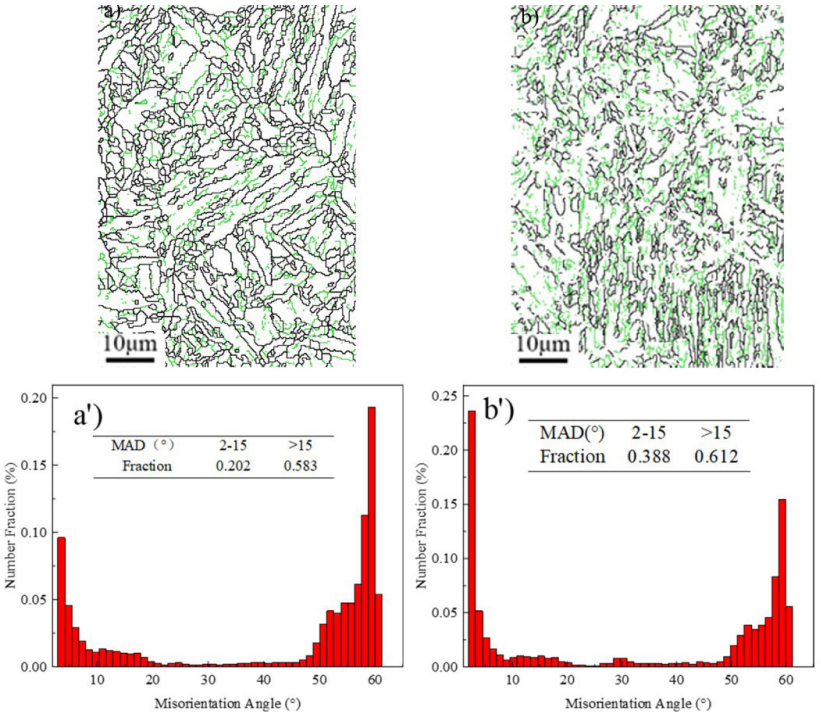

Figure 10. Grain boundary map and orientation angle distribution curves of the material surface before and after USRP treatment (a) and (a') untreated specimens; (b) and (b') USRP-treated specimens.

$$N_v = \frac{H_v - H_{v0}}{H_v} = \frac{K_0}{K}\sqrt{\frac{\rho}{\rho_0}} - 1 \quad (4)$$

Where K is a numerical factor related to the dislocation structure and distribution, edge-type dislocation K=1-v (Poisson's ratio); G is the shear modulus of elasticity; ρ_0, ρ is the surface dislocation density before and after processing. H_{v0} is the initial hardness, and N_v is the hardness after processing.

The principle of dislocation density hardening is shown in the following equation:

$$\sigma = M\alpha ub\sqrt{\rho} \quad (5)$$

Transformed to

$$\sqrt{\rho} = \frac{\sigma}{M\alpha ub} \quad (6)$$

Where M is the Taylor factor, u is the shear modulus, b is the Burgers vector, and α is the material constant, generally about 0.3.

Bringing Equation 6 into Equations 3, 4 yields

$$H_v = \frac{Gb_1\sigma}{MK\alpha ub} \quad (7)$$

$$N_v = \frac{K_0\sigma}{MK\alpha ub\sqrt{\rho}} - 1 \quad (8)$$

In the USRP process, the increase of plastic deformation caused dislocation sliding, and the dislocation sliding needs to overcome a specific resistance, which is the macroscopic expression of the flow stress in the deformation. At the same time, the rise of dislocation density will cause the rise of resistance, so the increase of dislocation density in the deformation process will increase the hardness and hardening of the material surface layer. It means that work hardening, workpiece flow stress, and dislocation density are closely related, and the three in the plastic deformation process affect each other.

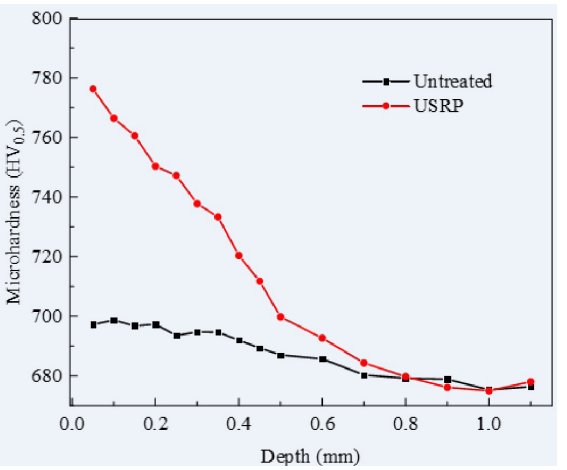

Figure 11. Cross-sectional hardness distribution of samples before and after USRP treatment.

3.5. Surface morphology and surface roughness

Figure 12 shows the sample surface's three-dimensional morphology and surface roughness before and after USRP

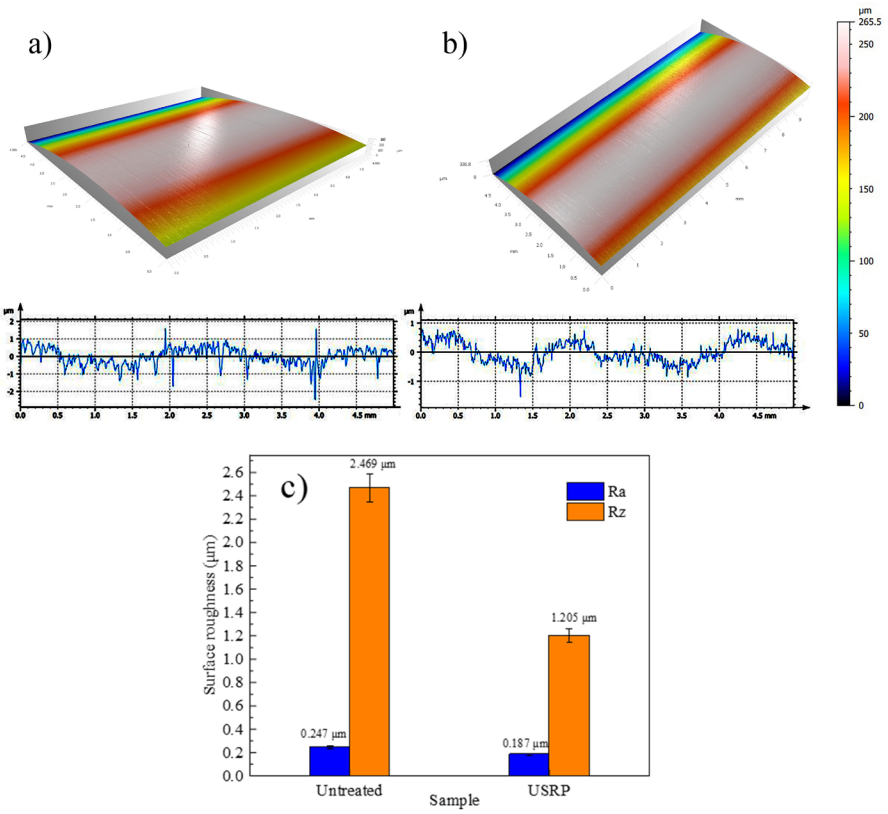

Figure 12. Three-dimensional morphology and surface roughness of sample surface before. and after USRP treatment: (a) untreated specimen; (b) USRP treated specimen; (c) comparison of Ra and Rz before and after USRP treatment.

treatment. The surface of the untreated sample has noticeable processing marks with surface roughness Ra=0.247μm and Rz=2.469μm. The surface roughness of the USRP-treated sample is Ra=0.187μm and Rz=1.205μm, and the surface morphology is relatively flat, forming a continuous and uniform plane, and the processing marks disappear. The above phenomenon can be attributed to the plastic deformation of the material under the action of ultrasonic rolling, which produces a peak and valley-cutting effect and a significant reduction in surface roughness.

The semi-empirical formula for calculating the surface stress concentration factor using surface roughness parameters is expressed as[37]:

$$K_t = 1 + n\sqrt{\lambda \frac{Rz}{\rho}} \quad (9)$$

Where Kt is the stress concentration factor, λ is the ratio of profile spacing to depth, and ρ is the effective radius of curvature of the profile valley. This relationship can be used to elucidate the effect of surface roughness on fatigue resistance performance. Therefore, USRP reduces surface roughness and is less likely to form stress concentrations, improving material fatigue performance and corrosion resistance.

Fatigue cracks usually originate at the surface, with tiny peaks and valleys on the surface, like many corners, nicks and cracks, which are the origin of stress concentrations. Under alternating loads, the presence of stress concentrations reduces fatigue strength. Therefore the surface has a great influence on the life of the part. The smoother the surface, the longer the time for fatigue cracks to sprout. The semi-empirical formula for calculating the surface stress concentration factor from the surface roughness parameter shows that USRP reduces the surface roughness and does not easily form stress concentrations, improving the fatigue resistance and corrosion resistance of the material.

3.6. XRD and corrosion resistance

The grain state and grain surface orientation were tested by X-ray diffraction. The results show that no new phases were found in the diffractograms of the three X-ray diffraction peaks corresponding to the α-Fe structure for (1 1 0), (2 0 0) and (2 1 1) after USRP treatment. The intensity of the diffraction peaks after USRP treatment were all significantly reduced, and their relative widths increased, which can be attributed to the high-frequency impact of USRP on the specimen surface, which refined the material grains and introduces residual compressive stresses on the specimen surface. The X-ray diffraction patterns of GCr15-bearing steel before and after USRP treatment are shown in Figure 13.

To facilitate a clear description of the differences in the X-ray diffraction images before and after USRP treatment, we determined the full width at half-peak (FWHM) values (Table 5). The results show a slight increase in the FWHM

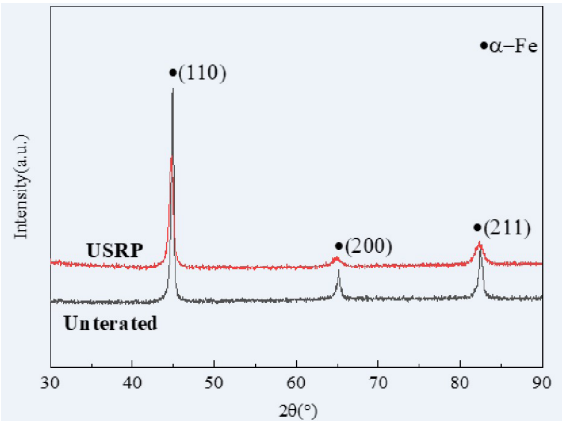

Figure 13. XRD spectra of GCr15 steel before and after USRP treatment.

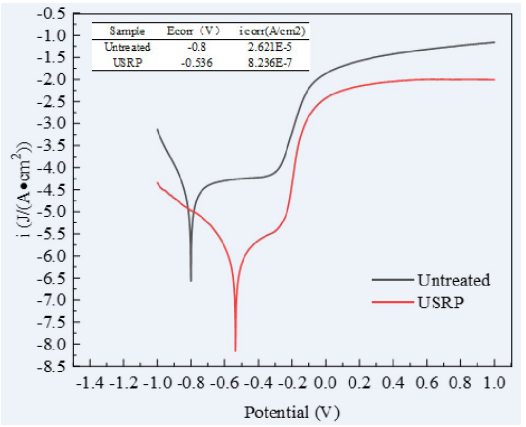

Figure 14. Tafel curves of GCr15 material surface before and after USRP.

Table 5. Full width at half peak (FWHM) values of (110) diffraction peaks of GCr15 steel.

Sample	2θ(°)	FWHM
Untreated	44.89	0.318
USRP	44.75	0.562

values of the diffraction peaks after USRP treatment, indicating grain refinement and an increase in residual compressive stress. During USRP, plastic strain occurs at the material surface, and surface crystal defects (twins, dislocations) are repeatedly annihilated and regenerated, generating more subgrain boundaries and achieving surface grain refinement, in agreement with the findings of microstructure and EBSD results (see Figures 6-9). It is noteworthy that the grain refinement improved hardness and corrosion resistance.

The Tafel plot (Figure 14) shows that the specimens before and after USRP treatment have similar polarization characteristics. The anodic passivation zone appears on the anodic polarization curve, and the cathodic polarization curve is smooth. The appearance of the anodic passivation zone is mainly due to the generation of dense oxide or other compound films on the anode surface, which covers the material surface and reduces the width of the anodic passivation zone significantly after the USRP treatment of the anode and solution. The significant reduction in the width of the anodic passivation zone may be due to the damage caused by the USRP treatment to the integrity of the oxide film on the material surface, resulting in the cracking and peeling of the oxide film, thus reducing the protective effect of the oxide film on the material.

The material's corrosion tendency and corrosion rate can be obtained quickly and easily using electrochemical experiments, where the self-corrosion potential (E_{corr}) and self-corrosion current density (I_{corr}) can determine the corrosion tendency and corrosion rate of the material, respectively. The specimen's self-corrosion potential (E_{corr}) and self-corrosion current density (I_{corr}) are shown in Figure 14. The self-corrosion potentials before and after USRP treatment are -0.8 V and -0.536 V, respectively. E_{corr} can reflect the degree of corrosion tendency of the material, and the larger the value, the smaller the corrosion tendency. I_{corr} can reflect the corrosion rate of the material, USRP treatment before and after the self-corrosion current density (I_{corr}) were 2.621×10^{-5} A/cm^2, 8.236×10^{-7} A/cm^2. The larger the value indicates, the faster the corrosion. After USRP treatment, the self-corrosion potential (E_{corr}) of the GCr15 steel surface increased, and the self-corrosion current density (I_{corr}) decreased by two orders of magnitude, indicating the corrosion resistance of all USRP-treated samples increased. There are two main reasons: On the one hand, the surface roughness affects the corrosion resistance of the specimen, which is less likely to be corrosion the lower the surface roughness of the sample.

On the other hand, the USRP treatment caused plastic deformation of the specimen surface; dislocations proliferated and moved within the grains. Dislocation entanglement occurred, which refined the surface grains of the specimen, resulting in an increase in the uniformity and denseness of the passivation film of GCr15 steel in 3.5% NaCl solution and a decrease in the rate of the anodic dissolution process to a shallower level. This conclusion is consistent with the above XRD results. In addition, the surface involvement of compressive stress also contributes to the material's corrosion resistance.

4. Conclusion

Ultrasonic surface rolling processing (USRP) is a promising method to extend the service life of GCr15 bearing steel. In this paper, the residual compressive stress and equivalent plastic strain distribution on the bearing steel surface were analyzed by the finite element method using GCr15 steel as the research object. The microstructure, hardness, surface roughness and corrosion resistance before and after USRP treatment were also characterized and analyzed. The results show that USRP treatment improves the surface microstructure and residual stress distribution of GCr15 steel, refines the surface grains, and obtains plastic deformation strengthening layer. This paper provides a reference for surface modification of GCr15 bearing steel and draws the following conclusions.

(1) The residual compressive stress tends to increase and then decrease with the increase of surface depth. The maximum value of residual compressive

stress is at the material subsurface. The maximum residual compressive stress reaches 367 MPa. The introduction of residual compressive stress delays the appearance and expansion of fatigue cracks and improves the material's service life.

(2) After USRP treatment, the material undergoes significant plastic deformation, forming a violent plastic deformation layer with a thickness of about 60 μm. The martensitic tissue on the top surface is broken and the tissue orientation becomes disordered, leading to grain refinement. The martensitic organization on the sub-surface of the material is elongated, and the deformation zone is formed by the interlacing of organizations in different directions within the grains.

(3) Based on the dislocation strengthening theory, the strengthening mechanism of the ultrasonic surface rolling processing (USRP) of GCr15 steel was analyzed. Under the coupling effect of static pressure and ultrasonic vibration, KAM increases from 0.95° to 1.29°. As a result, the dislocation activity becomes more intensive, and many high-density dislocation entanglements form dislocation walls and dislocation cells. The dislocation walls and dislocation cells rotate to form sub-grain boundary and low-angle grain boundaries, leading to an increase in the percentage of LAGB. Surface grain refinement is also the main reason for the increased hardness of the material.

(4) After the USRP treatment, the self-corrosion potential (E_{corr}) of the GCr15 steel surface was increased (from -0.8 V to -0.536 V). The self-corrosion current density (I_{corr}) was reduced by two orders of magnitude (from 2.621×10^{-5} A/cm^2 to 8.236×10^{-7} A/cm^2), resulting in a significant improvement in corrosion resistance. This improvement was achieved by the synergistic effect of surface grain refinement, low surface roughness, and residual compressive stress layer.

5. Acknowledgments

This study was supported by Natural Science Foundation of Shandong Province (ZR2021ME182); State Key Laboratory of Material Forming and Mould Technology Open Fund Project(P12); National Natural Science Foundation of China (52105377); and the Major Project of the Science and Technology Enterprise Innovation Program of Shandong Province, China (Grant No. 2022TSGC2108 and 2022TSGC2402).

6. References

1. Yin F, Hua L, Mao H, Han X. Constitutive modeling for flow behavior of GCr15 steel under hot compression experiments. Mater Des. 2013;43:393-401.
2. Guo D, Zhang P, Jiang Y, Song C, Tan D, Yu D. Effects of surface texturing and laminar plasma jet surface hardening on the tribological behaviors of GCr15 bearing steel. Tribol Int. 2022;169:107465.
3. Yin F, Hua L, Mao H, Han X, Qian D, Zhang R. Microstructural modeling and simulation for GCr15 steel during elevated temperature deformation. Mater Des. 2014;55:560-73.
4. Kinner-Becker T, Hettig M, Sölter J, Meyer D. Analysis of internal material loads and Process Signature Components in deep rolling. CIRO J Manuf Sci Technol. 2021;35:400-9.
5. Bagherifard S, Fernandez-Pariente I, Ghelichi R, Guagliano M. Effect of severe shot peening on microstructure and fatigue strength of cast iron. Int J Fatigue. 2014;65:64-70.
6. Zine PU, Joshi PK. Inducing compressive residual stress to minimize effect of crack generation by using controlled shot peening process. Mater Today Proc. 2022;72(Pt 3), 870-877.
7. Kumar S, Chattopadhyay K, Singh V. Effect of ultrasonic shot peening on LCF behavior of the Ti–6Al–4V alloy. J Alloys Compd. 2017;724:187-97.
8. Rai PK, Pandey V, Chattopadhyay K, Singhal LK, Singh V. Effect of ultrasonic shot peening on microstructure and mechanical properties of high-nitrogen austenitic stainless steel. J Mater Eng Perform. 2014;23(11):4055-64.
9. Jia W, Hong Q, Zhao H, Li L, Han D. Effect of laser shock peening on the mechanical properties of a near-α titanium alloy. Mater Sci Eng A. 2014;606:354-9.
10. Fu J, Zhu Y, Zheng C, Liu R, Ji Z. Enhanced plasticity of bulk metallic glass in different aspect ratios via laser shock peening with multiple impacts. Opt Laser Technol. 2016;83:43-8.
11. Wang H, Song G, Tang G. Enhanced surface properties of austenitic stainless steel by electropulsing-assisted ultrasonic surface rolling process. Surf Coat Tech. 2015;282:149-54.
12. Yasuoka M, Wang P, Zhang K, Qiu Z, Kusaka K, Pyoun Y-S, et al. Improvement of the fatigue strength of SUS304 austenite stainless steel using ultrasonic nanocrystal surface modification. Surf Coat Tech. 2013;218:93-8.
13. Pegues J, Roach M, Scott Williamson R, Shamsaei N. Surface roughness effects on the fatigue strength of additively manufactured Ti-6Al-4V. Int J Fatigue. 2018;116:543-52.
14. Zhao W, Liu D, Zhang X, Zhou Y, Zhang R, Zhang H, et al. Improving the fretting and corrosion fatigue performance of 300M ultra-high strength steel using the ultrasonic surface rolling process. Int J Fatigue. 2019;121:30-8.
15. Luo X, Ren X, Jin Q, Qu H, Hou H. Microstructural evolution and surface integrity of ultrasonic surface rolling in Ti6Al4V alloy. J Mater Res Technol. 2021;13:1586-98.
16. Qin T, Ao N, Ren X, Zhao X, Wu S. Determination of optimal ultrasonic surface rolling parameters to enhance the fatigue strength of railway axle EA4T steel. Eng Fract Mech. 2022;275,108831.
17. Liu Z, Zhao H, Zhang C, He Z, Ji V. Investigation on the evolution of residual stress in ultrasonic surface rolling treatment-processed 18CrNiMo7-6 alloy steel. Trans Indian Inst Met. 2022
18. Ren S, Zhang Y, Zhao Y, An Z, Xue F, Yao J, et al. Enhanced Surface properties and microstructure evolution of Cr12MoV using ultrasonic surface rolling process combined with deep cryogenic treatment. J Mater Eng Perform. 2019;28(2):1132-40.
19. Wu D, Lv H, Wang H, Yu J. Surface micro-morphology and residual stress formation mechanisms of near-net-shaped blade produced by low-plasticity ultrasonic rolling strengthening process. Mater Des. 2022;215:110513.
20. Wang P, Guo H, Wang D, Duan H, Zhang Y. Microstructure and tribological performances of M50 bearing steel processed by ultrasonic surface rolling. Tribol Int. 2022;175:107818.
21. Zou Y, Li J, Liu X, He T, Lu J, Li D, et al. Effect of multiple ultrasonic nanocrystal surface modification on surface integrity and wear property of DZ2 axle steel. Surf Coat Tech. 2021;412:127012.
22. Dang J, Zhang H, An Q, Lian G, Li Y, Wang H, et al. Surface integrity and wear behavior of 300M steel subjected to ultrasonic surface rolling process. Surf Coat Tech. 2021;421:127380.
23. Yang J, Liu D, Ren Z, Zhi Y, Zhang X, Zhao R, et al. Grain growth and fatigue behaviors of GH4169 superalloy subjected to excessive ultrasonic surface rolling process. Mater Sci Eng A. 2022;839:142875.

24. Luo Y, Qin T, Jia X, Hu Y, Li C, Mu G, et al. Fatigue life enhancement of foreign object impacted railway axle EA4T steel with surface shot peening. Eng Fail Anal. 2022;142:106782.
25. Valera HY, Bhavsar SN. Experimental investigation of surface roughness and power consumption in turning operation of EN 31 alloy steel. Procedia Technology. 2014;14:528-34.
26. Fu P, Chu R, Xu Z, Ding G, Jiang C. Relation of hardness with FWHM and residual stress of GCr15 steel after shot peening. Appl Surf Sci. 2018;431:165-9.
27. Li Y, Lian G, Geng J, Song C, Chen D, Wang H. Effects of ultrasonic rolling on the surface integrity of in-situ TiB2/2024Al composite. J Mater Process Technol. 2021;293:117068.
28. Ye C, Telang A, Gill AS, Suslov S, Idell Y, Zweiacker K, et al. Gradient nanostructure and residual stresses induced by Ultrasonic Nano-crystal Surface Modification in 304 austenitic stainless steel for high strength and high ductility. Mater Sci Eng A. 2014;613:274-88.
29. Saraf L. Kernel average misorientation confidence index correlation from FIB Sliced Ni-Fe-Cr alloy surface. Microsc Microanal. 2017;17(S2):424-5.
30. Zhao K, Gao T, Yang H, Hu K, Liu G, Sun Q, et al. Enhanced grain refinement and mechanical properties of a high–strength Al–Zn–Mg–Cu–Zr alloy induced by TiC nano–particles. Mater Sci Eng A. 2021;806:140852.
31. Zribi Z, Ktari HH, Herbst F, Optasanu V, Njah N. EBSD, XRD and SRS characterization of a casting Al-7wt%Si alloy processed by equal channel angular extrusion: dislocation density evaluation. Mater Charact. 2019;153:190-8.
32. Wang N, Chen Y, Wu G, Zhao Q, Zhang Z, Zhu L, et al. Non-equivalence contribution of geometrically necessary dislocation and statistically stored dislocation in work-hardened metals. Mater Sci Eng A. 2022;836:142728.
33. Xu X, Zhang J, Liu H, He Y, Zhao W. Grain refinement mechanism under high strain-rate deformation in machined surface during high speed machining Ti6Al4V. Mater Sci Eng A. 2019;752:167-79.
34. Li B, Zhang S, Fang Y, Zhang J, Liu Z. Deformation behaviour and texture evolution of martensite steel subjected to hard milling. Mater Charact. 2019;156:109881.
35. Gashti SO, Fattah-alhosseini A, Mazaheri Y, Keshavarz MK. Effects of grain size and dislocation density on strain hardening behavior of ultrafine grained AA1050 processed by accumulative roll bonding. J Alloys Compd. 2016;658:854-61.
36. Shi H, Zong N, Le J, Li S, Huang G, Li J, et al. Strain hardening versus softening: anisotropic response of strain hardening-softening transition in a polycrystalline zirconium alloy at room temperature from dislocation viewpoint. Mater Sci Eng A. 2022;847:143344.
37. Arola D, Williams CL. Estimating the fatigue stress concentration factor of machined surfaces. Int J Fatigue. 2002;24(9):923-30.